science.sciencemag.org/content/371/6526/280/suppl/DC1

Supplementary Materials for

Driving energetically unfavorable dehydrogenation dynamics with plasmonics

Katherine Sytwu, Michal Vadai, Fariah Hayee, Daniel K. Angell, Alan Dai, Jefferson Dixon, Jennifer A. Dionne*

*Corresponding author. Email: jdionne@stanford.edu

Published 15 January 2021, *Science* **371**, 280 (2021)
DOI: 10.1126/science.abd2847

This PDF file includes:

Other Supplementary Material for this manuscript includes the following:
(available at science.sciencemag.org/content/371/6526/280/suppl/DC1)

Movie S1 (.mp4)

Contents

1 Materials and Methods

1.1 Fabrication of Sample

1.1.1 Palladium Nanorod Synthesis

Penta-twinned palladium nanorods are colloidally synthesized using a modified version of a previously published procedure (*20*).

First, a 10mM H_2PdCl_4 solution is made by dissolving 8.9mg of $PdCl_2$ in 208µL of 0.48M HCl, and then diluting with 4.792mL of water. The solution is then sonicated until all the salt dissolves.

To grow the nanorods, 5mL of a 100mM CTAB solution is heated to 90°C in a glass scintillation vial. The solution is kept under constant stirring at 350rpm in an oil bath. Then, 250µL of the above 10mM H_2PdCl_4 solution, 200µL of a 100mM KI solution, 14-16µL of a 10mM $AgNO_3$ solution, and 175µL of a 0.48M HCl solution are sequentially added. The resulting length of the nanorods was found to be extremely sensitive to the amount of $AgNO_3$, and so in practice, multiple batches are made simultaneously with various amounts of $AgNO_3$. After waiting 5 minutes, 400µL of 100mM ascorbic acid is added to the solution, and the reaction is allowed to sit for 1.5 hours at 90°C.

To clean the nanoparticles, four 1mL aliquots of the reaction mixture are centrifuged at 3800rpm for 10 minutes. The supernatant is then removed, and 500µL of Milli-Q water is added to each centrifuge tube. The four aliquots are then combined into two aliquots, and centrifuged again for 3800rpm for 10 minutes. This procedure is repeated until one final aliquot is cleaned. After this final centrifugation and supernatant removal, around 200µL of Milli-Q water is added until the mixture is medium brown in color.

1.1.2 Gold Nanobar Fabrication

An array of 60-90nm x 4µm rounded Au nanobars placed 1µm apart was fabricated on a 30nm thick, 100µm-wide single-window silicon nitride (Si_3N_4) membrane (SPI Supplies). First, the grids are UV-ozone-cleaned for 3 minutes to promote adhesion of the subsequent polymethyl methacrylate (PMMA) layer. Next, PMMA 495k molecular weight 4% in anisole (MicroChem Corp.) is spin-coated onto the grids at 4500rpm for 40 seconds. After baking at 180°C for 3 minutes, the PMMA is exposed in a JEOL JBX-6300FS EBL system, followed by 46 seconds of development in a 3:1 isopropyl alcohol (IPA): methyl isobutyl ketone (MIBK) solution. Next, a 1-1.5nm adhesive layer of Ti and 10-15nm of Au are deposited in an Angstrom e-beam evaporator. After lift-off in acetone overnight, the grids are then transferred to a carrier wafer for atomic layer deposition (ALD). The grids undergo 25 cycles of plasma SiO_2 ALD using tris[dimethylamino]silane (3DMAS) and oxygen plasma in a Fiji F202 system from Cambridge Nanotech to conformally coat the sample with 2nm of SiO_2. The SiO_2 acts as a spacer layer to prevent any charge transfer effects from metal-metal contact as well as welding between the Pd nanorods and Au nanobars upon illumination. It also allows for dropcasted nanorods to be evenly distributed across the sample due to uniform hydrophilicity. The SiO_2 thickness is verified visually using high-resolution TEM imaging and ellipsometry measurements to be between 1.8-3nm.

1.1.3 Sample Preparation

The SiO_2-coated TEM grid with fabricated Au nanobars is plasma-cleaned in air plasma at 10W for 1 minute, and then 7µL of the cleaned Pd nanorod solution is dropcasted on the grid. After 6 minutes, the remaining liquid is wicked off with a Kimwipe, and the sample is stored in a glovebox under argon gas until needed for the experiment.

Due to their pentatwinned strained nature, these long Pd nanorods support multiple defects. While our dehydrogenation measurements without illumination and some of our illumination videos suggest that defects do not play a significant role in determining the nucleation site of the α-phase, we still screen all potential Au-Pd nanorod pairs via 200kV TEM imaging (on a FEI Tecnai TEM) such that we only study Au-Pd pairs with no visible defects near the Au-Pd crossing.

Before inserting the sample in the TEM, the sample is placed in the TEM holder and kept in a vacuum environment for 30 minutes before plasma cleaning with a 25/75 Ar/O_2 plasma at 50W for 1 minute to remove excess surfactant.

1.2 Optical Microscopy

1.2.1 Dark Field Optical Imaging and Spectroscopy

The fabricated TEM grids were placed on a Zeiss Observer inverted microscope with a dark field reflector cube. The samples were illuminated by a tungsten halogen lamp (HAL100, Zeiss), and the resulting image was recorded by a CCD camera. The scattered light was then sent to a Princeton Instruments Acton 2560i spectrometer with a PI PyLoN CCD cooled to -120°C. For each spectra, we subtracted a background signal (of 2nm of SiO_2 on top of 30nm of Si_3N_4 on top of Si), taken away from the patterned area, and then applied flatfield correction which accounts for the non-uniform spectral illumination intensity of the halogen lamp.

1.3 Electron Microscopy

1.3.1 Imaging Conditions

All experiments and imaging are done with a FEI Titan environmental TEM operated at 80kV. For all in-situ experiments, the electron dose is set to 10e/Å^{2}s at 24kX magnification. This is chosen as a trade-off between achieving enough signal (see dark field imaging details below) and keeping the dose rate low enough to avoid beam effects (see electron beam effects below). To keep the overall dosage minimal, the column valves are closed in between measurements.

1.3.2 Displaced Aperture Dark Field Imaging

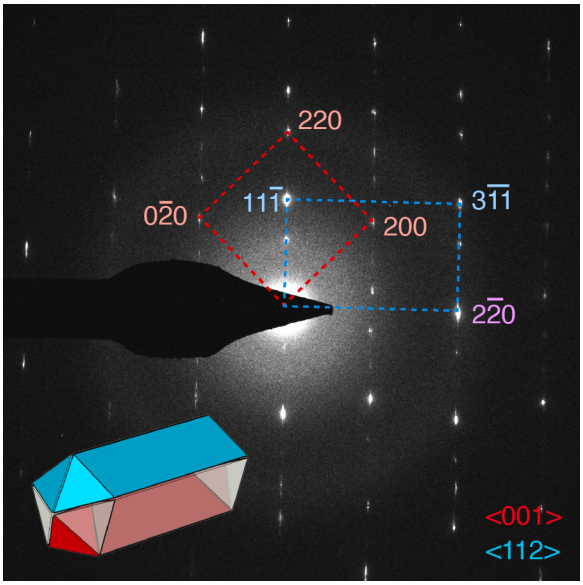

Figure S1: Selected area diffraction pattern of a single pentatwinned Pd nanorod. The diffraction pattern from Figure 2A replicated here with one unit cell of the <001> (red) and <112> (blue) zone axes highlighted and labeled. The schematic inset on the bottom left shows the crystallite(s) of the pentatwinned nanorod that contribute to each diffraction pattern.

The diffraction pattern of a pentatwinned nanorod consists of two overlaid diffraction patterns: a <100> zone axis pattern from the bottom crystallite and a <112> zone axis pattern from the top two crystallites. The rest are double diffraction points, originating from electrons which diffract from both [100] and [112] crystallites. While we do find that all crystallites undergo the phase transformation simultaneously (see section on dehydrogenation without illumination), we generally only monitor one crystallite at a time to be safe (i.e. choosing from the <100> pattern).

For successful displaced aperture dark field imaging, there needs to be a balance between two factors: 1) high signal in the objective aperture when the particle is in the hydrogen-rich β-phase, and 2) lack of signal when the particle is in the hydrogen-poor α-phase. Note that having signal represent β-phase and lack of signal represent α-phase is an arbitrary choice. We could've also chosen

the place the objective aperture slightly outside the β-diffraction point and switched our convention such that lack of signal would represent β-phase and signal would represent α-phase.

To maximize signal, one needs to choose a bright diffraction point. This rules out the double-diffraction spots, as they arise from a 2nd-order interaction with the sample, and so are generally dimmer. This also means that one would like to choose lower-order diffraction points as they have higher signal than higher-order diffraction points. The brightest diffraction point is usually the $[2\bar{2}0]$ diffraction point, which has signal from both the <100> and <112> diffraction patterns; however, we avoid tracking the dark field image from this diffraction point in the off chance that the separate crystallites behave differently and we cannot distinguish differences between them.

On the other hand, to maximize contrast, one needs to choose a diffraction point that will completely move out of the objective aperture upon dehydrogenation (i.e. lack of signal when in the α-phase). This necessitates both careful placement of the objective aperture and a diffraction point that moves relatively far in k-space. As the diffraction rings will expand $\sim 2-3\%$ upon dehydrogenation, the higher-order diffraction points will shift relatively further than the lower-order diffraction points; therefore, a higher-order diffraction point would ensure better contrast between the two phases and less reliance on exact objective aperture placement which is subject to human error.

Therefore, we need to choose a diffraction point that is only in the <100> diffraction pattern, is a lower-order diffraction point with strong signal, but is of high-enough order to detect some change in position upon dehydrogenation. We therefore generally choose the [220] diffraction point (labeled in Figure S1, highlighted in Figure 2A), which also has no nearby diffraction points which could enter the objective aperture upon dehydrogenation.

Finally, for successful data collection on nucleation site, the resulting dark field image needs to cover the entire nanorod length. Since the nanoparticles are dropcasted onto an uneven grid of nanobars, the Pd nanorods may not always lie flat relative to the electron beam. We rotate the sample (axis along the Au nanobar length) until the entire nanorod length is visible in the dark field image.

By choosing to study a process in which the lattice contracts, we do not have to worry about only capturing heating effects, as that would cause the diffraction pattern to contract and stay within the objective aperture. We do have to consider that we might just be capturing the formation of defects (i.e. a twist). However, from previous studies of the diffraction pattern during hydrogenation and dehydrogenation, we know that this defect formation accompanies the phase transition (*21*). To verify all of our claims on the phase transition, we double check the phase of the particle before and after every data acquisition period by measuring the diffraction pattern length.

The resulting dark field images have a number of artifacts. Since the objective aperture is moved to the diffraction point, our imaging conditions are off-axis, leading to some ghost images/smearing of the dark field image in the direction of the diffraction point. These aberrations do not affect our results or resolution, and help align images during post-processing (as they do not disappear upon dehydrogenation). Similarly, since our Au nanobars are polycrystalline and the Au reciprocal lattice is smaller than that of Pd, we occasionally also capture dark field images of Au crystallites, which can be seen in Figure 2B. These Au crystallite dark field images are also used to align images during post-processing. Finally, for the Pd nanorods that are on top of the Au nanobar, the regions that overlap with the Au nanobar have much less signal since Au is strongly scattering.

1.3.3 Electron Energy Loss Spectroscopy (EELS) Maps

EELS maps are collected by raster-scanning a monochromated scanning TEM beam (FWHM of 0.15eV) across the sample with collection time per pixel of 0.05s. After collection, EEL spectra are aligned using simultaneously collected low-loss spectra of the zero-loss peak, and normalized to the total number of counts collected.

Our EELS processing scheme is depicted in Figure S2. To remove the zero-loss peak, a background signal is created by averaging the aligned and normalized EEL spectra at the four corners of the EELS map. This background signal is then subtracted from all pixels to remove the zero-loss peak and other substrate background signals. Next, to extract the transverse plasmon mode, the EELS map goes through non-negative matrix factorization, a blind deconvolution method that can isolate plasmonic modes, with the number of modes chosen via principal component analysis. The transverse mode is then chosen from the extracted modes and smoothed. The EELS map insets are created by calculating the weight of the transverse plasmon mode in each pixel spectra.

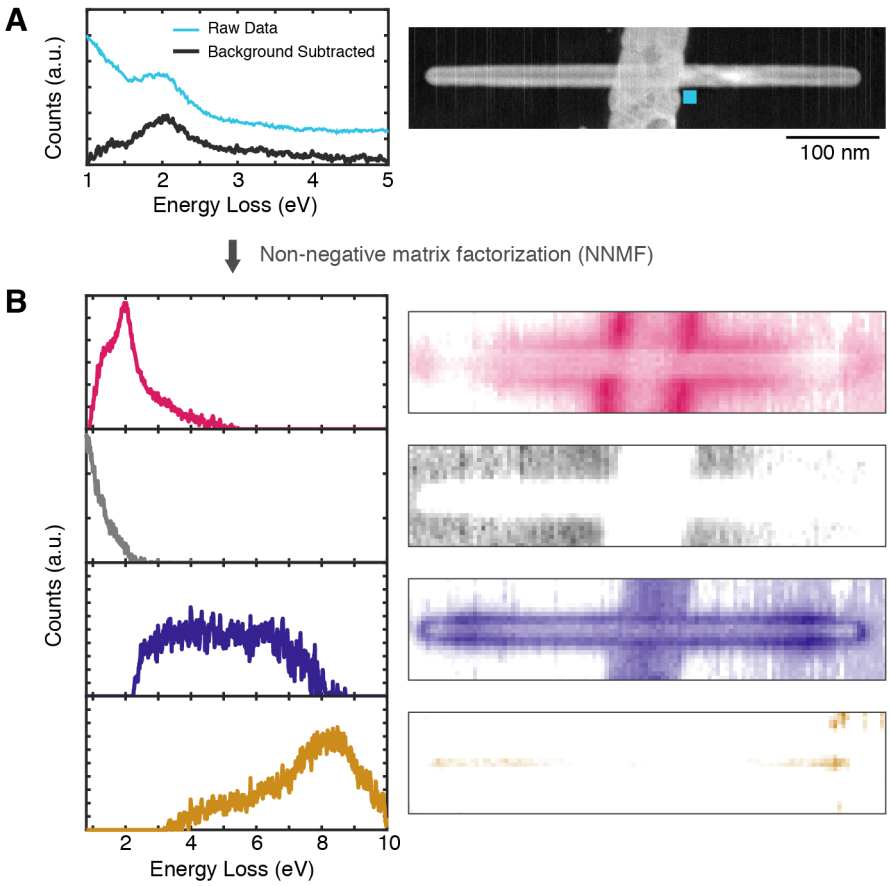

Figure S2: Electron Energy Loss Spectroscopy (EELS) processing procedure. (A) The raw data (blue) and background subtracted (black) electron energy loss spectra taken near the Au nanobar edge, as shown by the blue box on the STEM image on the right. The background substracted data is then fed to a non-negative matrix factorization (NNMF) algorithm. (B) The NNMF algorithm decomposes the spectrum into four spectra (left). We then calculate the weight of each mode at each spatial location, creating the spatial distribution of the mode (right). From the combination of the spectra and spatial distributions, we can identify the different modes. For example, the Au-Pd system shown here (same as Figure S12A) has the following modes: transverse LSPR mode (pink), background (grey), Pd nanorod plasmon and Au interband transitions (purple), and Pd bulk plasmon (yellow).

1.3.4 Electron Dose Effects

Both incident illumination and the electron beam can excite local surface plasmon resonances; light must be of the specific resonant wavelength, but the electron beam acts as a broadband source and can excite any and all plasmons. Therefore, throughout all of our measurements, we are constantly exciting all LSPRs (transverse, longitudinal, corner, etc.).

Despite this, we believe that since our electron dose is kept constant and low ($10e/Å^2s$), there are minimal beam effects. If the electron-beam excited LSPR was strong, then we would observe dehydrogenation even under non-resonant illumination. However, in our illumination studies, we only observe dehydrogenation under resonant illumination. Similarly, we have never seen spontaneous dehydrogenation caused by just the electron-beam. The sample is often under electron-beam irradiation for over 180s in preparation for illumination studies; therefore, light illumination can cause dehydrogenation while electron-beam irradiation for a similar amount of time cannot, or in other words, the LSPR excited by illumination is stronger than that created by the electron beam.

While the electron-beam induced LSPR plays a minimal role in our illumination studies, it does affect control measurements of the dehydrogenation phase transition without illumination for PdH_x nanorods coupled to a Au nanobar (see below section on additional dehydrogenation statistics).

From previous studies, higher beam doses seem to only increase phase transition kinetics and not

modify the mechanism or behavior (*12*), which we also observe in our experiment. Our setup can only track one crossed Au-Pd pair at a time, but illuminates the entire TEM grid. Therefore, for a given hydrogen pressure, all Au-Pd pairs are illuminated (and many share the same LSPR resonance) but only one Au-Pd pair is imaged by electrons, allowing us to isolate out any electron beam effects. We found that if the illumination time is short ($\lesssim$ 30 seconds) and the hydrogen pressure high enough, then only the Au-Pd pair that has been imaged by electrons will undergo a phase transition. Otherwise, for longer illumination times or at lower hydrogen pressures, the non-imaged Au-Pd pairs also fully dehydrogenate, or show partial dehydrogenation (only part of the nanorod is in α-phase). These observations suggest that while the electron beam plays a small role in accelerating the phase transition, it is still light illumination that drives the phase transition.

1.4 Dehydrogenation Experiments

1.4.1 Before Experiments

After inserting the sample into the microscope, the sample is heated to 323K under 400Pa of hydrogen gas (99.9999% purity from Praxair) to reduce the palladium oxide layer. The particles are then brought down to 246K and then fully cycled (hydrogenated and then dehydrogenated) twice to avoid capturing the anomalous behavior that has been reported during the first hydrogenation cycle.

1.4.2 Without Illumination

Since dehydrogenation kinetics are extremely slow (*22*), Pd nanorods support co-existing states (i.e. do not show a first-order phase transition) (*16*) and DADF is only accurate when the nanoparticle is in focus, we accelerate the phase transition by working at a higher temperature and constantly dropping the hydrogen pressure.

To track the natural dehydrogenation dynamics of the Pd nanorods, we use a TEM cryo holder (Gatan) and set the temperature to 263K. We start by verifying that the nanorod is hydrogenated (via its diffraction pattern) at ∼380 Pa. Then, we monitor the particle via DADF as we continually drop the hydrogen pressure by closing the leak valves by a set amount, and repeating every time the nanorod stops drifting (the sample decreases in temperature due to the pressure drop and then heats up to maintain a constant 263K temperature, which causes sample drift). The nanorods generally start to dehydrogenate around 60-120Pa of hydrogen gas.

The exposure time for each frame was 0.15sec in order to balance signal to noise and temporal resolution. Movies were taken with the screen-capture software in Digital Micrograph.

1.4.3 With Illumination

The sample is placed in a cryo-cathodoluminescence holder (Gatan) and set to 246K. After the Pd nanorod is verified to be hydrogenated (via its diffraction pattern), we drop the pressure to the pressure of interest and then wait for 30 minutes to ensure that the Pd nanorod is stably in the β-phase. For nanorods that show rehydrogenation upon turning off illumination (see section on rehydrogenation behavior below), we do not wait 30 minutes between measurements as the nanorods are presumed to be stable in the β-phase.

We limit our illumination time to 180s; if no phase transition is detected within this acquisition period, we record that there is no nucleation site.

Video capture specifications were the same as the without illumination case (0.15sec frame exposure).

1.4.4 Optics and Cathodoluminescence Holder

We illuminate our sample by fiber-coupling a pulsed, supercontinuum laser (NKT Photonics) into the bottom mirror of a cryo-cathodoluminescence (CL) holder. The supercontinuum laser has a ∼100ps pulse length, a repetition rate of 78MHz, and is coupled to a spectrometer which acts as a variable bandpass filter. For 50nm bandpass illumination, the resulting center illumination wavelength is not the maximum illumination wavelength, and so we report the weighted average illumination wavelength.

For each wavelength and bandpass used, we measure the average power that is coupled into the fiber (i.e. power into the CL holder) using a power meter (ThorLabs). The reported average power is then calculated by multiplying the recorded average power with the measured coupling efficiency of

the bottom CL port (10%, via photodiode measurements within the CL holder). Incident intensity is calculated by assuming a 200μm diameter beam spot (which corresponds to the measured 200μm CL hot spot). Note that illumination intensity is not uniform across the ∼200μm beam spot, and so actual incident intensity at each Au-Pd pair will also vary, even within a single sample. Therefore, it is very difficult to make conclusive comparisons of effects due to illumination intensity across multiple Au-Pd pairs, and we can only make conclusions based off of measurements done on a single Au-Pd pair within the same experimental session.

1.4.5 Pressure-Dependent Measurements

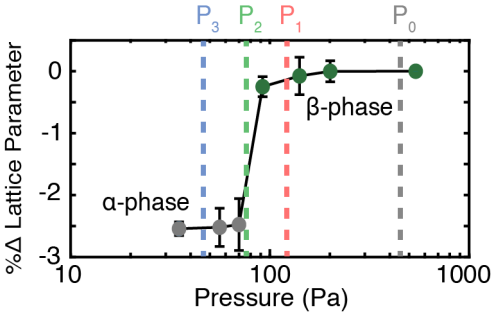

Figure S3: Schematic of the pressure-dependent measurements, showing how the pressures sampled the nanorod at various locations on its isotherm.

Figure S3 schematically outlines how the pressure-dependent measurements were performed. The gas pressure was first set to P_0 to get the particle stably in β-phase, and then lowered to P_1. After waiting 30 minutes for near-equilibrium, the sample is illuminated on resonance and the nucleation behavior is recorded. If the particle remains in α-phase after illumination (due to the hysteresis), the pressure is brought back up to P_0 before repeating this process for pressures P_2, P_3, etc.

1.4.6 Isotherm Measurements

Dehydrogenation isotherms were taken at 263K and calculated via changes in the diffraction pattern, using similar methods reported in previous papers (*15,21*). After waiting 30 minutes at the pressure of interest, the smallest selected-area-electron-diffraction (SAED) aperture was used to take diffraction patterns at three points of each nanorod: the two tips and the middle. The order in which these measurements were taken varied per pressure step. After diffraction patterns are taken of all nanorods, the pressure is dropped to the next pressure of interest. Overall, the nanorods stay at each pressure step for around one hour.

To create the isotherms, the distance between three pairs of diffraction points are measured and the percentage change in lattice parameter relative to the hydrogenated case at the highest pressure is calculated. The average percentage change is then plotted, with the error bar signaling two standard deviations.

1.5 Computational Methods

1.5.1 Gibbs Free Energy Calculation

The change in Gibbs free energy, ΔG, is positive for the endothermic PdH_x dissociation phase transformation. To calculate the Gibbs free energy as a function of hydrogen concentration, as seen in Figure 1B, we use the mean-field model with finite-size and subsurface saturation effects introduced by Griessen et al (*23*). Note that this is for a coherent phase transition and so does not accurately describe our (likely incoherent) system.

Briefly outlined, we define the total H concentration in the Pd lattice to be $x_{total} = (1-g)x_c + gx_s$ where g is the volume fraction of surface sites, x_c is the concentration in the core, and x_s is the concentration in the saturated surface/subsurface. For a cylinder, we derive g to be

$$g = 1 - \frac{(r-t)^2(L-2t)}{r^2 L}$$

where r is the radius, L is the length, and t is the thickness of the saturated shell. For our calculations, we take the Pd nanorod dimensions to be $r = 12$nm, $L = 450$nm, and $t = 1$nm.

Then, the total free energy is

$$\Delta G = (1-g)\Delta H_{\text{core}} + g\Delta H_{\text{surf}} - T\big((1-g)\Delta S(x_c,T) + g\Delta S(x_s,T)\big)$$

where ΔH_{core}, ΔH_{surf}, and ΔS are as defined in reference (*23*) and duplicated below:

$$\begin{aligned}
\Delta H_{\text{core}} &= \Delta H_{\infty,\text{core}}(x_c,x_s) + \Delta H_{\text{electronic}}(x_c) + \Delta H_{\text{st}} \\
\Delta H_{\text{surf}} &= \Delta H_{\infty,\text{surf}}(x_c,x_s) + \Delta H_{\text{electronic}}(x_s) + \Delta H_{\text{st}} \\
\Delta S(x,T) &= 71.78 - 0.0702T + 6.88\times10^{-5}T^2 - 2.89\times10^{-8}T^3 \\
&\quad + 29.23x - 9.15x^2 - 54.83x^3[\text{J/molH}]
\end{aligned}$$

where

$$\Delta H_{\infty,\text{core}}(x_c,x_s) = \Delta H^{\infty}(T) + (1-\gamma g)\Delta H_{\text{elastic}}(x_c)(1-\frac{w}{d}) + \gamma g\Delta H_{\text{elastic}}(x_s)(1-\frac{w}{d})$$
$$\Delta H_{\infty,\text{surf}}(x_c,x_s) = \Delta H^{\infty}_{\text{surf}} + (1-\gamma(1-g))\Delta H_{\text{elastic}}(x_s)(1-\frac{w}{d}) + \gamma(1-g)\Delta H_{\text{elastic}}(x_c)(1-\frac{w}{d})$$

and the bulk contributions to enthalpy are defined as

$$\begin{aligned}
\Delta H^{\infty}(T) &= 14770 + 12.94T[\text{J/molH}] \\
\Delta H_{\text{elastic}}(x) &= 63640x - 40170x^2 + 9740x^3[\text{J/molH}] \\
\Delta H_{\text{electronic}}(x) &= -7248x - \frac{87955x^{4.1791}}{\xi + x^4}[\text{J/molH}]
\end{aligned}$$

Note that d is a variable representing the finite size dimension. In ref (*23*), the model system is a cube so their finite dimension is the edge length. Here, our finite dimension is chosen to be $d = 2r$.

In ref (*23*), both x_c and x_s are solved for since there are two separate equations governing the thermodynamics. Here, as we are just trying to calculate the free energy (and hence only have one equation), we can only choose one variable. We decide to numerically set x_s to an offset rectified linear function:

$$x_s = \max(0.51, x_c)$$

representing a constantly saturated surface which increases in concentration as more hydrogen is introduced into the core.

1.5.2 FEM Simulation of Plasmon-Induced Heating

The timescales of electron-electron scattering (10s of fs) and electron-phonon scattering (1-5ps) in Au are much shorter than our ∼100ps laser pulse; therefore, we can forgo the two temperature model of hot electron dynamics and directly model our heat response such that it is dominated by absorption (*24*). Therefore, our heat source is defined as:

$$q(r,\omega) = \frac{\omega}{c}\text{Im}[\epsilon(r,\omega)]I(r,\omega)$$

where $I(r,\omega)$ is the local intensity of light and ϵ is the complex dielectric function. As we want to study the transient evolution of the temperature of the Au-Pd system, we simplify this equation by assuming that we only have incident light of a single frequency and modulate its intensity as a Gaussian pulse in time:

$$\tilde{q}(r,t) = \frac{\omega_0}{c}\text{Im}[\epsilon(r,\omega_0)]I(r,\omega_0)\sqrt{2\pi}\sigma\exp-\frac{(t-t_0)^2}{2\sigma^2} \tag{1}$$

where σ=50ps sets our pulse width and t_0=100ps sets the time of maximal pulse intensity. To implement this, we linearize this process and model optical heating in two steps: first solving an optics simulation (in the frequency domain), whose solution feeds into a transient heating simulation (time domain).

Using COMSOL multiphysics, we model our structure using the same parameters as our FDTD simulations: a Au nanobar with 75nm width and 15nm thickness, surrounded by 2nm of SiO_2 and on top of a 30nm Si_3N_4 substrate, with a Pd nanorod of 500nm length and 25nm diameter crossed on top. Half-spheres are added to the Pd nanorod ends to round out the tips. As seen in our FDTD simulations, the choice of nanobar dimensions should not affect the heating simulations other than spectrally shifting the resonance. We choose the length of the Au nanobar to be 700nm to reduce the size of our mesh and computation time and solve for the optical response with periodic Floquet-Bloch boundary conditions. We choose the domain size to be large enough to consider the nanoparticle to be isolated from the periodic boundaries, therefore modeling a semi-infinite domain with the computational simplicity of a periodic domain. Consequently, the spacing between neighboring periodic domains ensures that the boundaries are isothermal in the thermal modeling and do not excite any lattice-modes in the optical modeling.

Due to the switch from a FDTD solver to a FEM solver, we first perform a frequency-sweep of the nanosystem's optical response to verify the LSPR peak position. We find that the resonant frequency is at 640nm, approximately the same as that found in our FDTD simulations. The cross-sectional field map of this response is plotted in Figure 1E.

1.5.3 Heating Simulation Parameters

Next, we run a time-dependent heating study in which the entire Au-Pd nanostructure is a heat source which follows Equation 1. In practice, the heat source is taken as the absorptive loss of each volumetric mesh component (calculated in the electromagnetic response) multiplied by a Gaussian function whose height is the peak intensity magnitude.

Since our heating simulations will give us an upper bound on any plasmonic heating (due to the approximation that all of illumination is exactly on resonance rather than across a bandwidth of frequencies and that we cannot account for active cooling of the substrate on the order of seconds), we set our peak intensity to the maximum recorded average power of around 3mW. Given that our illumination spot has a diameter of $\sim$ 200µm, we have a Gaussian pulse, and only the transverse polarization of light contributes to heating, our resulting peak intensity is $I_0 = 1.73 \times 10^7$ W/m^2.

We set the rectangular boundaries to be adiabatic (no heat flux); they are placed 700nm away from the nanostructure such that the heat transfer through the substrate does not reach the edges by the end of the temporal simulation (i.e. the simulation does not reach thermal equilibrium). To verify, we tracked the temperature of a heat source as we varied the thermal isolation boundary position, and found that temperature profile over time does not change as long as the boundary is further than $\sim$450nm from the heat source.

Our choices of thermal constants are listed below:

Material	Thermal Conductivity [W/mK]	Density [kg/m^3]	Specific Heat Capacity (c_p) [J/kgK]
Si_3N_4	3	3170	800
Au	87.58	18900	130
Pd	14.12	12300	240
SiO_2	1.4	2650	700

Table S1: Material parameters used for finite element modeling.

1.5.4 Molecular Dynamics Simulations

Simulations were done using the LAMMPS molecular dynamics package. Our simulations utilized an embedded atom method (EAM) interatomic potential, which has been shown to correctly model and replicate the strain-induced thermodynamic miscibility gap for both nanoparticle and bulk PdH_x (*25*). For simplicity, our PdH_x nanorod is modeled as a rectangular nanobar with 20nm width (taken from our experimental median nanorod width) and varying lengths of 38.9nm, 77.8nm, and 155.6nm. Since we are not able to model the full length of the Pd nanorod, we show calculations for various lengths to demonstrate how our findings persist even with different nanorod lengths.

To model the different nucleation configurations, the volume fraction in α-phase for each configuration is constant (6%) such that comparisons between simulations only captures the configuration's effect on the systems energy. We assume that the phase-front in all configurations is (100).

After constructing each configuration, the structure is relaxed by potential minimzation via the Polak-Ribiere conjugate gradient algorithm, and is iterated until a maximum force of 1e-6 eV/Angstrom is achieved. We then calculate the total energy, U, at 0K and divide by the total number of atoms. Since there is no kinetic energy and the measurement is taken at 0K, our total energy is essentially equivalent to the Gibbs free energy. Therefore, any changes in energy should reflect changes due to different α and β spatial distributions. Note that the absolute value and sign of the simulated Gibbs free energy is meaningless in this case since the measurements are taken at 0K (compared to our experimental measurements at 246K) and the zero point energy is chosen arbitrarily. We can, however, interpret our results qualitatively by comparing the different energies against each other.

2 Supplementary Text

2.1 Wide-Field View of TEM Grid

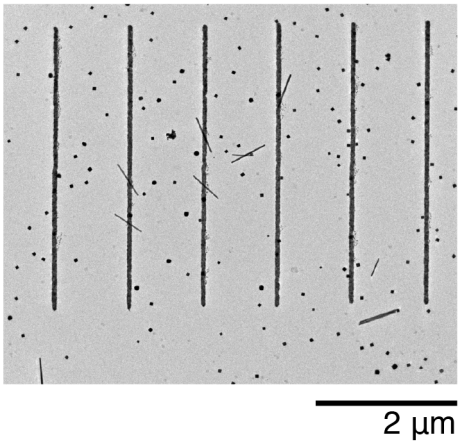

Figure S4: Wide-field view of the TEM grid, showing the fabricated Au nanobars and the Pd nanoparticles strewn about. Crossed-bar samples can be seen on the second and third nanobars from the left.

2.2 FDTD Simulations of the Plasmonic Response of the Au-Pd Structure

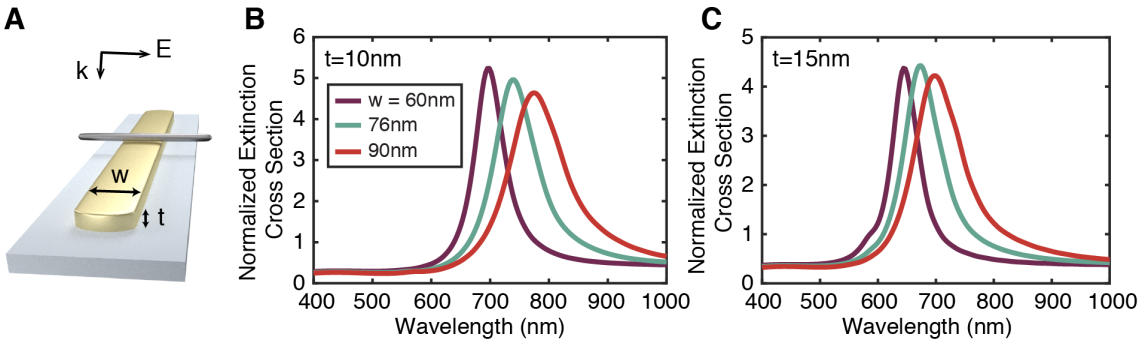

Figure S5: FDTD Simulations of the normalized extinction cross section of the Au-Pd system with varying Au nanobar dimensions. (A) Schematic of the FDTD setup: a single Au nanobar with rounded corners and varying width (w) and thickness (t), surrounded by 2nm of SiO_2 and a Pd nanorod crossed on top, all on top of a 30nm thick Si_3N_4 block. The incoming illumination is polarized such that the transverse LSPR will be excited. (B,C) The computed normalized extinction cross section when the Au nanobar is (B) 10nm and (C) 15nm in thickness, with nanobar widths of 60nm (purple), 76nm (turquoise), and 90nm (red).

Using Lumerical, a commercial finite difference time domain (FDTD) electromagnetic solver, we compute the normalized extinction cross section of our Au-Pd structure. To reduce memory constraints and make sure that our simulation converged in a reasonable time, the Au nanobar length was shortened from 4μm to 1.3μm; this is an appropriate approximation since the nanobar length should not affect the transverse LSPR by too much. While the (experimental) incident illumination is unpolarized, the Au nanobars are long enough (4μm) such that the transverse LSPR is the only resonant feature in the visible regime. Therefore, we only simulate the incident electric field being polarized in the transverse direction.

The Au-Pd system is modeled as 30nm Si_3N_4 substrate with a Au nanobar coated with 2nm of SiO_2 and a Pd nanorod of 500nm length and 25nm diameter crossed on top (see Figure S5A). We add half-discs to the ends of our Au nanobar (which is also reflected in the lithography design) to round the corners. This results in only a single plasmon resonance when illuminating with transverse illumination; otherwise, we would see spectrally distinct transverse and corner LSPR modes. Note that we do not include the 1-1.5nm Ti adhesion layer in these simulations; this adhesion layer has been shown to mainly broaden the LSPR peak though can slightly shift the resonant wavelength (*26*).

In Figure S5, we see that increasing the thickness blue-shifts the LSPR peak, agreeing with previous calculations of Au nanobar LSPR modes (*27*), and that increasing the the Au nanobar width red-shifts the LSPR peak, agreeing with our dark field and cathodoluminescence spectra in Figure 1C.

As Figure 1C shows the experimental spectra for a Au nanobar array of 10nm thickness and varying widths, we can make some comparisons between Figure 1C and Figure S5B. First, while the trends are similar, the exact LSPR peak positions are blue-shifted in the FDTD simulations compared to the experimental measurements. This is likely due to using bulk Si_3N_4 material data for our substrate as the permittivity of the substrate highly affects peak position. Second, we do not see any additional peaks in the experimental spectra of the ensemble structure (unpolarized incident light) compared to the FDTD simulations of the single structure (transverse polarized light), confirming that we do not have any array modes or longitudinal LSPR modes in the visible regime.

2.3 Dehydrogenation Without Illumination

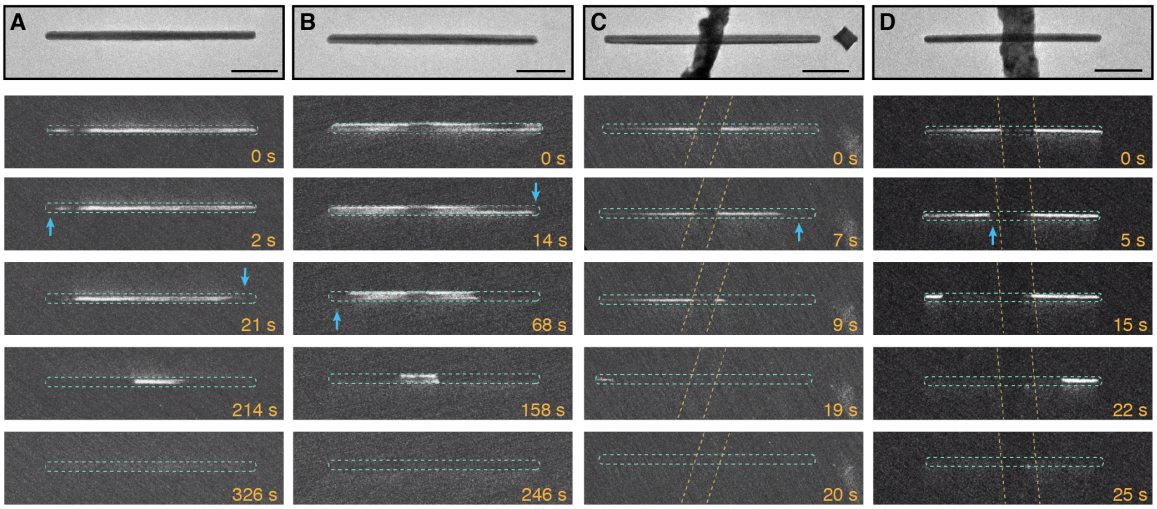

Figure S6: Additional screenshots of dehydrogenation mechanisms without illumination. TEM images and DADF screenshots of dehydrogenation dynamics without illumination for (A) a 454nm long nanorod with a defect, (B) a 432nm long nanorod with two defects (with its DADF image tracking two crystallites simultaneously), (C) a 463nm long nanorod crossed with a Au nanobar which shows single tip nucleation, and (D) a 371nm long nanorod crossed with a Au nanobar which shows middle nucleation. Blue arrows indicate nucleation location of the new α-phase. Timestamps reference time from first observation of a α-phase nucleation site. All scale bars are 100nm.

Figure S6 shows screenshots from additional dehydrogenation videos without illumination. In Fig. S6A, we see that a nanorod with a visible defect (the lack of signal in the DADF image at 0s) will still

nucleate the dehydrogenated phase from both ends of the nanorod. In Fig. S6B, we track the [111] diffraction point, which results in a dark field image of two crystallites. We see that both crystallites dehydrogenate simultaneously which corresponds with our previous observations that each crystallite does not operate independently (*16*). Therefore, if we are tracking the behavior of one crystallite, we are tracking the behavior of the entire nanorod. Note that in Figure S6B, we also see that despite two defect sites, the nanorod still prefers to nucleate at both ends of the nanorod.

Figure S6C and D show the dehydrogenation dynamics of the Au-Pd system under no illumination; Figure S6C shows single tip nucleation while Fig. S6D shows middle nucleation near the hot-spot. While there is no illumination, we are still exciting the plasmonic response of the Au nanobar due to the influence of the electron beam. This is confirmed by the accelerated kinetics of the phase transformation in Figs. S6C and D compared to A and B. Therefore, we see similar behavior and phase transformation mechanisms here as we do under illumination.

Due to the continual and non-uniform drop in pressure over time, we cannot examine the kinetics of this phase transformation under these dark conditions. We also cannot compare these kinetics to that of the illuminated case as we are also working at a higher temperature (263K vs 246K). Due to the nature of this measurement, our reported kinetics are a lower bound for (i.e. faster than) the actual kinetics.

2.4 Electron-Beam Induced SiO_2 Radiative Defect

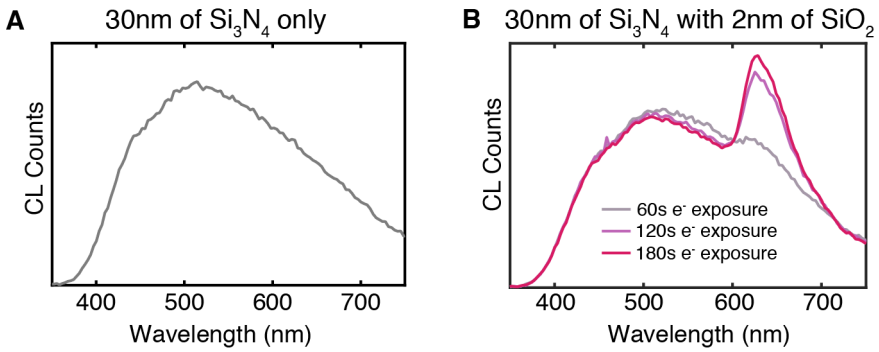

Figure S7: The electron-beam induced radiative defect in SiO_2. (A) Cathodoluminescence (CL) spectra of a blank 30nm Si_3N_4 TEM grid at 80kV, showing a broad background peak from 400-700nm. (B) CL spectra of a blank 30nm Si_3N_4 TEM grid with 2nm of ALD-grown SiO_2 taken after multiple electron-beam total exposure times at 80kV. As total electron dosage increases, we see the appearance of a peak at around 630nm, which suggests a radiative electron-beam induced defect. This 630nm peak corresponds with the observed 630nm peak in the CL spectra in Figure 1C for the 60nm width nanobars. We hypothesize that this defect is why we see a shifted CL spectra for the 60nm width nanobars in Figure 1C. The DF optical spectra in Figure 1C show a LSPR peak around 615nm; since the LSPR is of higher energy than the radiative defect, we hypothesize that the LSPR radiatively decays via coupling into this radiative defect, hence why it shows a CL peak at 630nm despite a LSPR peak around 615nm. For the wider nanobars, the LSPR is at a lower energy (redder) than the 630nm radiative defect; therefore the defect does not affect the optical response as much.

2.5 Rehydrogenation Behavior after Illumination Turns Off

Occasionally (in 6 of 27 studied particles), we observe that after an illumination-driven transition into the α-phase, once the laser is turned off, the nanorod would immediately start to rehydrogenate back into the β-phase, as shown in Figure S8. In this example, illumination is turned on at 0s and the PdH_x nanorod starts to dehydrogenate into the α-phase (i.e. the signal disappears). At 20s, the phase transition into α-phase is complete and we turn off the laser. Immediately after illumination is turned off, as seen in the screenshot at 20.63s, the PdH_x nanorod starts to rehydrogenate into β-phase again, nucleating the new β-phase at the right tip. The full phase transition into β-phase continues, including a second nucleation of the β-phase at the opposite tip about 12s after the laser is turned off, until the nanorod is fully back into the β-phase.

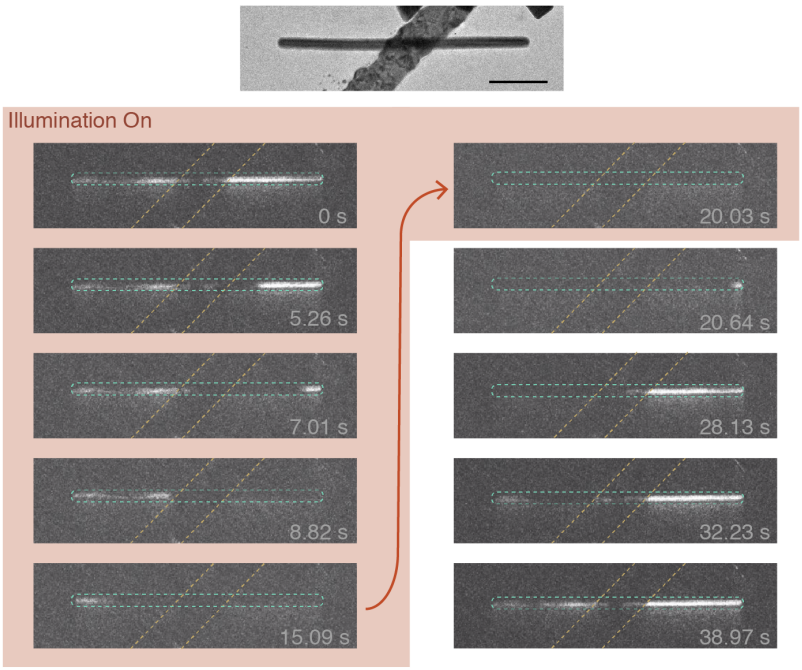

Figure S8: Example of rehydrogenation behavior. TEM image and DADF screenshots showing the dehydrogenation (upon resonant illumination of 650nm with 20nm bandwidth) into α-phase and subsequent rehydrogenation (when the laser is turned off at 20s) into β phase of a 430nm long nanorod. The H_2 is kept constant at 101Pa throughout this measurement. Scale bar is 100nm.

While we only show one example here, we note that we also see a variety of rehydrogenation mechanisms, including full rehydrogenation starting from a single tip, middle, or defect as well as partial rehydrogenation such that only part of the nanoparticle is in β-phase. Understanding the rehydrogenation behavior is beyond the scope of this study, but by observing rehydrogenation, we can verify two of our claims: 1) indeed, LSPRs excited via illumination (and not solely via electron-beam) cause dehydrogenation as our phase transition relies on the presence of the laser and 2) the PdH_x nanorods are stably in the β-phase such that the LSPR excitation is not only influencing the nanorod to transform via an energetically-unfavorable mechanism, but also pushing it into an unfavorable state. At these environmental conditions (H_2 pressure and temperature), without LSPR excitation, the nanorods would not naturally transform into the α-phase.

2.6 Cycling Effects

To verify that the illumination-dependent behavior does not change over multiple cycles, we plot the nucleation behavior as we vary the illumination conditions over time (Figure S9). Clearly, even after middle nucleation is observed under resonant conditions (measurement numbers 6, 8, 13, etc.), lower illumination power (measurement numbers 7 and 9) as well as off-resonant illumination (measurements 16-21) does not initiate a reaction. Additionally, repeating the measurements under same illumination conditions (measurement numbers 6, 11, 13, and 15) results in the same behavior.

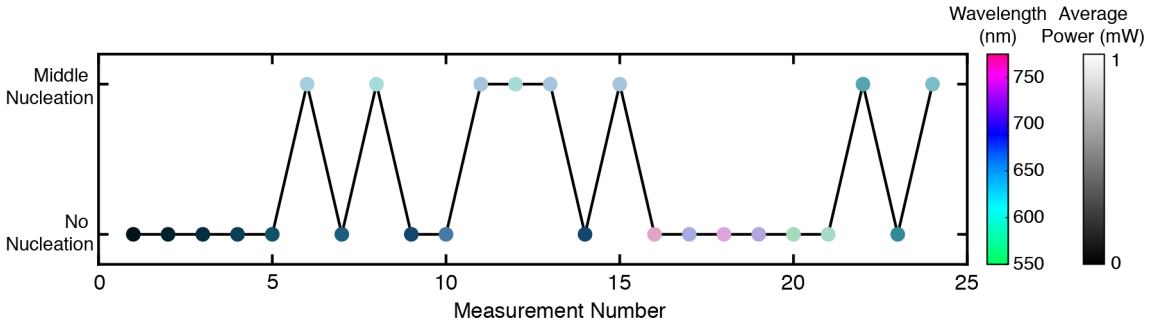

Figure S9: Measurements over time with varying illumination conditions. Figure 3B replotted, showing the measurements as a function of time. Illumination parameters are denoted by color; wavelength is represented by hue while average power is represented (nonlinearly) by saturation and brightness. For exact illumination conditions, see Figure 3B.

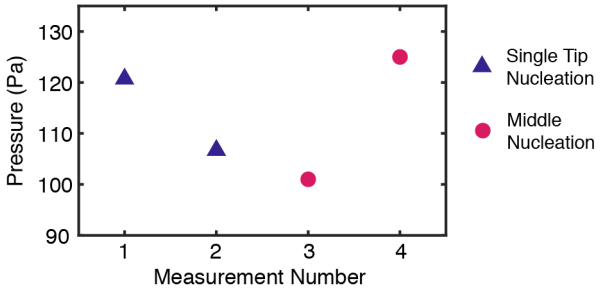

Figure S10: Measurements over time with varying pressure. Nucleation site under resonant illumination as H_2 pressure is decreased and then increased.

However, while illumination can repeatedly initiate the same type of phase transition, we find that certain phase transition properties do change over multiple cycles. For instance, in Figure S10, we show an example of a nanorod which changed its pressure-dependent nucleation behavior after undergoing middle nucleation. At 121Pa, under resonant illumination, the nanorod undergoes tip nucleation. We then decrease the pressure to 101Pa and under the same illumination conditions, we observe middle nucleation. When pressure is increased to 125Pa, higher than the original observation of tip nucleation, we would expect to see tip nucleation or nothing happening as we are further away from the natural dehydrogenation pressure. However, we now see middle nucleation despite the same illumination conditions as before, indicating that the Pd nanorod has changed. Note that this data is the same data as shown in Figure S14A particle number 10; therefore, when doing pressure-dependent measurements, we only take data as the pressure is decreased to avoid capturing these effects.

We hypothesize that this changed behavior comes from defect formation which alters the particle's thermodynamic behavior. Our previous studies of palladium hydrogenation found that single crystalline nanoparticles retain their single crystallinity after multiple cycles (*12, 21*) and polycrystalline nanorods showed similar behavior after three cycles of hydrogenation (*16*). However, in our case, many of these nanorods are being cycled numerous (15+) times, and "forced" into a phase transition dynamic that is energetically unfavorable. We hypothesize that the repeated cycling and/or the extreme unfavorableness of middle nucleation causes additional defects to form in the Pd nanorod (which generally already supports a number of defects) which then make it more energetically favorable to nucleate in the middle of the nanorod.

2.7 Wavelength-Dependence of Reaction Times

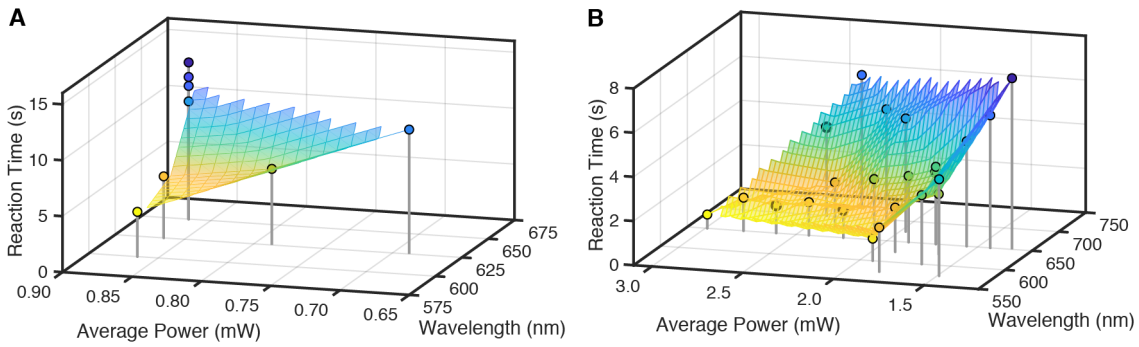

Figure S11: Illumination wavelength and power dependence of the phase transition time. The total phase transition time (measured from observation of a nucleation site until entire nanoparticle has transformed) under various illumination conditions for the nanoparticle in (A) Figure 3A,B and (B) Figure 3C,D. The mesh plane and colors are meant as a guide-to-the-eye.

Mapping out the phase transition kinetics as a function of illumination wavelength and power gives a more accurate identification of the LSPR resonance and effect (*12*). Figure S11 shows the wavelength and power-dependence of the reaction time (time for the phase transition to complete) for the measurements taken in Figure 3B (left) and S12B (right). Lower reaction times imply a faster reaction, or increased kinetics. We see in Figure S11A, which plots the kinetics of the measurements in Figure 3B, that the plasmon resonance at 599nm is more apparent due to the faster kinetics with 600nm illumination compared to other wavelengths (625nm, 650nm) with the same average power of 0.87mW. Similarly, in Figure S11B, which plots the kinetics of the measurements in Figure S12B, we observe similar low reaction times at illumination wavelengths of 600nm and 650nm, which corresponds with the observation of the LSPR around 626nm.

Interestingly, we observe a wavelength-dependent reaction time in this system, which we do not see in our previously reported Au-antenna PdH_x-nanocube-reactor system (*12*). This could be due to the order of magnitude difference in the size of the reactor ($\sim$ 50nm for the nanocube versus $\sim$ 500nm for the nanorod). Accordingly, if we scale our reaction times by 10x, the differences in kinetics are on the order of 1sec, which is similar to the variations that we had observed. Alternatively, these variations in reaction time could point towards the role of heating in the phase transition.

We note that multiple effects other than LSPR properties do contribute to phase transition kinetics, including defect concentration, defect formation, H_2 partial pressure, and stability of co-existing phases. Since our measurements are done on the same nanoparticle at the same and/or similar H_2 partial pressures, we can normalize out some effects across measurements of the same nanoparticle (i.e. H_2 partial pressure) but not all (i.e. defect formation and concentration).

2.8 Additional Wavelength-Dependent Measurements

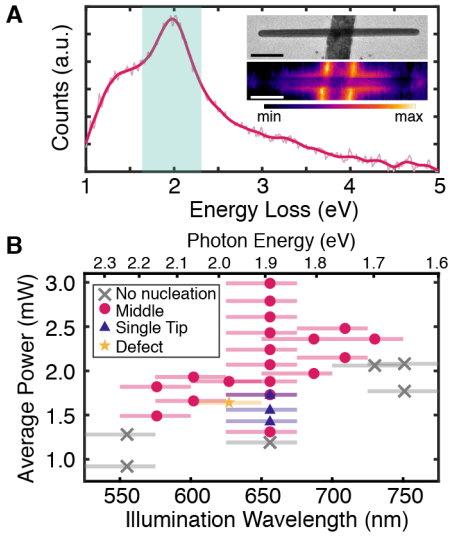

Figure S12: Additional wavelength-dependent measurements. (A) EELS of the LSPR mode (pink is smoothed spectra) shows a peak resonance at 1.98eV (626nm), with the corresponding TEM image and EELS map as an inset. Blue shaded region indicates illumination range of measurements in (B). Scale bars are 100nm. (B) Nucleation site of the α-phase for various illumination wavelengths and powers on the Au-PdH_x system in (A) at 84Pa of H_2 gas. Bars denote illumination bandwidth. This system demonstrates middle nucleation over a wider range of illumination wavelengths compared to Figure 3, likely because of the higher average illumination power. Here, we observe that off-resonant illumination at 700-725nm can also induce a phase transition, but requires higher illumination powers than on-resonance illumination at 600-650nm.

2.9 Single-particle Isotherms of the Dehydrogenation Phase Transition

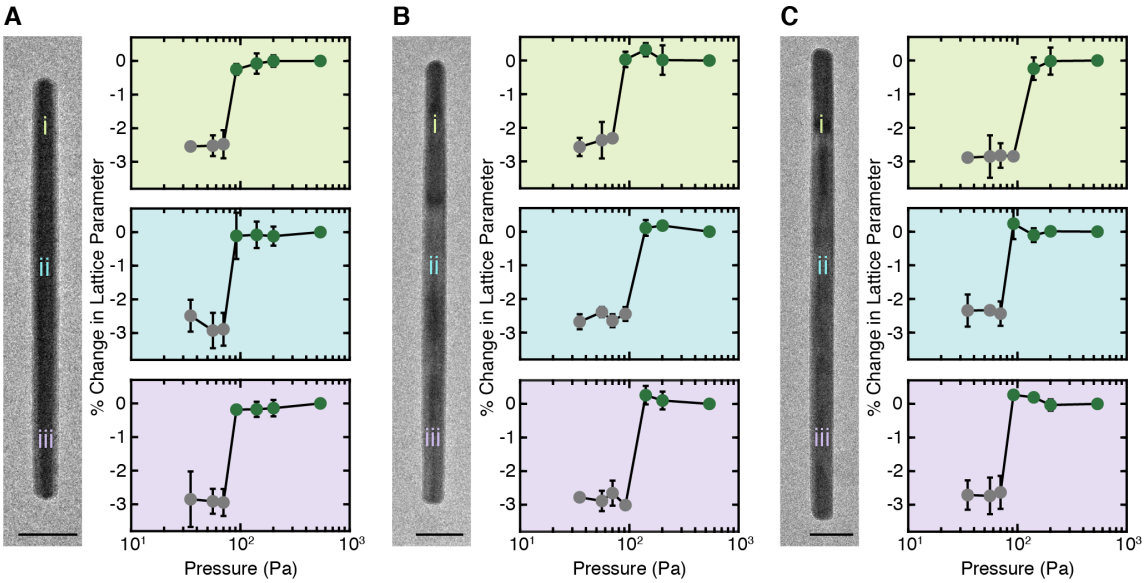

Figure S13: Single particle isotherms. Isotherms for the dehydrogenation phase transition for three nanorods of length (A) 354nm, (B) 469nm, and (C) 541nm. The isotherms are derived from selected area diffraction patterns taken at three areas of each nanorod, marked by i (green), ii (blue), and iii (purple). Green dots indicate β-phase while grey dots indicate α-phase. The isotherm shown in Figure S3 is the same as A.i. Scale bars are all 50nm.

As a reference for the near-equilibrium behavior of the PdH_x nanorods, we take isotherms for the dehydrogenation phase transition in individual nanorods of varying length, three of which are plotted in Figure S13.

We find that at 246K, the nanorods are stably in the β-phase down to 141Pa of hydrogen gas. At 91Pa, some of the longer nanorods start to dehydrogenate into α-phase as seen in Figure S13B.ii and iii as well as Figure S13C.i. The longer nanorods support co-existing α and β-phases, identical to our findings on hydrogenation behavior in similar nanorods (*16*). By 70Pa, all nanorods (10 nanorods of length varying from 350-540nm) have transitioned to α-phase.

These natural dehydrogenation pressures are higher than what we have observed when setting up our illuminated pressure-dependent studies (see Figure 4 and Figure S14). This suggests that these pentatwinned nanorods are not in their equilibrium state after sitting at a specific pressure point for ~30min. However, that inference is not supported by our occasional observance of rehydrogenation which suggests that the particle is stably in the β-phase. Therefore, we hypothesize that in our illuminated dehydrogenated experiments, the nanorods are in a kinetically-trapped β-phase. In those experiments, after the nanorods are hydrogenated at a high pressure, the pressure is lowered to the pressure of interest and the particle is allowed to sit in that environment for 30min, while in the isotherms, the nanorods are sitting in a slowly diminishing hydrogen environment for a couple of hours (each data point takes ~1hr: 30min to wait for near equilibrium, and 30min for data collection) and therefore more likely to reach full equilibrium.

2.10 Full Dataset of Pressure-Dependent Measurements

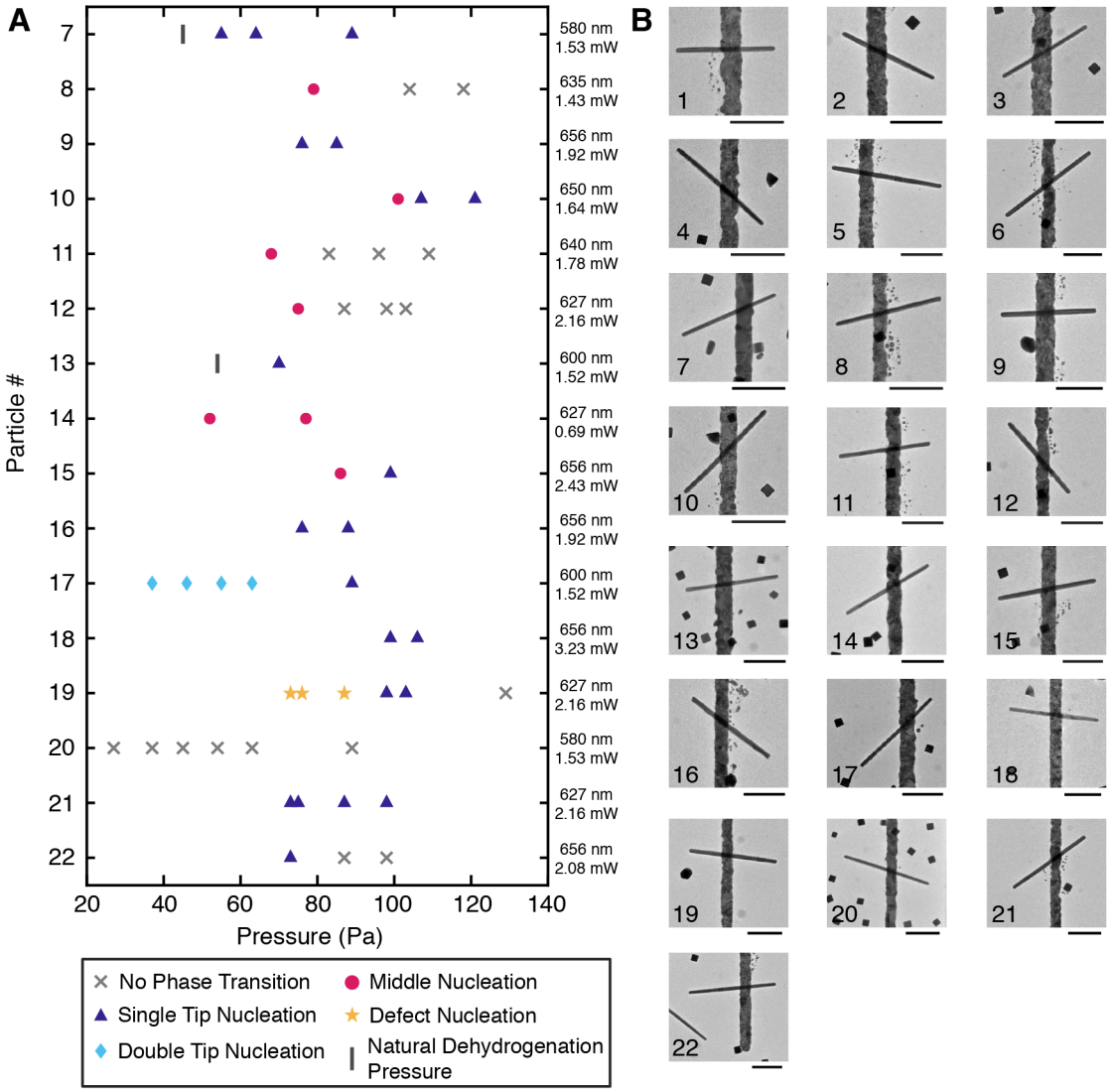

Figure S14: Additional statistics for pressure-dependent nucleation behavior. (A) Pressure-dependent nucleation site dynamics for 16 additional nanoparticles under resonant illumination. Illumination conditions (average wavelength and power) are provided in the right column. Defect nucleation (seen in particle 19) refers to nucleation at a site other than the tip(s) or at the Au-PdH_x intersection. (B) TEM images of all 22 particles (6 from Figure 4A and 16 from (A)) with particle number indicated in the bottom left corner. All scale bars are 200nm.

2.11 Experimental Parameters for Figure 4A and Figure S14

Particle #	Center Wavelength	Bandwidth	Illumination Power	Pd Nanorod Length
1	670nm	20nm	1.76mW	367nm
2	640nm	20nm	1.78mW	389nm
3	670nm	20nm	1.76mW	401nm
4	650nm	20nm	1.64mW	424nm
5	640nm	20nm	1.78mW	531nm
6	640nm	20nm	1.78mW	551nm
7	580nm	20nm	1.53mW	385nm
8	635nm	20nm	1.43mW	404nm
9	650nm	50nm	1.92mW	408nm
10	650nm	20nm	1.64mW	430nm
11	640nm	20nm	1.78mW	440nm
12	625nm	50nm	2.16mW	446nm
13	600nm	20nm	1.52mW	447nm
14	625nm	50nm	0.69mW	452nm
15	650nm	50nm	2.43mW	468nm
16	650nm	50nm	1.92mW	469nm
17	600nm	20nm	1.52mW	481nm
18	650nm	100nm	3.23mW	504nm
19	625nm	50nm	2.16mW	507nm
20	580nm	20nm	1.53mW	525nm
21	625nm	50nm	2.16mW	535nm
22	650nm	50nm	2.08mW	584nm

Table S2: Illumination parameters and nanorod characteristics of the data presented in Figure 4A and S14.

2.12 Plasmonic Heating in the Crossed-Bar System

To better understand the spatial distribution of plasmonic heating in our antenna-reactor system, we use finite element modeling to simulate the plasmon-induced heating and dissipation in our system under pulsed illumination. Our system has a Gaussian "laser pulse" that peaks at 100ps with a maximum intensity of 1.73×10^7 W/m^2, corresponding to our maximum recorded average power of 3mW (see Methods above). We find that the temperature increase initially follows the spatial profile of the EM enhancement (Figure S15A) and then spatially broadens over time (Figure S15B) due to heat transfer to the gas environment and substrate.

To analyze the instantaneous heating effects, we plot out the thermal response of the Pd nanorod at various points down its length through the center as a function of time, as seen in Figure S15C. Interestingly, we see that the spatial heating profile changes over time. Right after the laser pulse, our structure has a single thermal hot spot in the middle of the nanorod despite there being two electromagnetic hot spots; as the structure cools, the heat diffuses and the temperature distribution becomes more uniform, though the two EM hot spots are still apparent at 1300ps. Due to our imaging conditions, we cannot differentiate between a phase transition nucleating in the middle of the Au-Pd intersection (thermal hot spot) or at one of the EM hot spots. Eventually at much longer timescales around 12.8ns, the heat has diffused through the entire nanorod length and the spatial heating profile is more Gaussian-like (inset of Figure S15D). We suggest that these various thermal spatial profiles could be utilized in future experiments to gain more insight into nucleation timescales and mechanism.

We calculate the heat profile for the Pd nanorod out to 12.8ns, or the time between sequential laser pulses in our experiment. In Figure S15D, we plot the temperature increase at the middle and tip of the Pd nanorod. After 12.8ns, the temperature difference between the middle and the tip decreases from a maximum of 374mK to a small but finite 3.2mK (Figure S15D inset).

Extrapolating this result to the ms timescale of our experiment requires unphysical linearization of the temporal response. Since this is the temperature difference after one pulse of illumination, we could multiply by the 78MHz repetition rate to approximate the temperature increase after 1

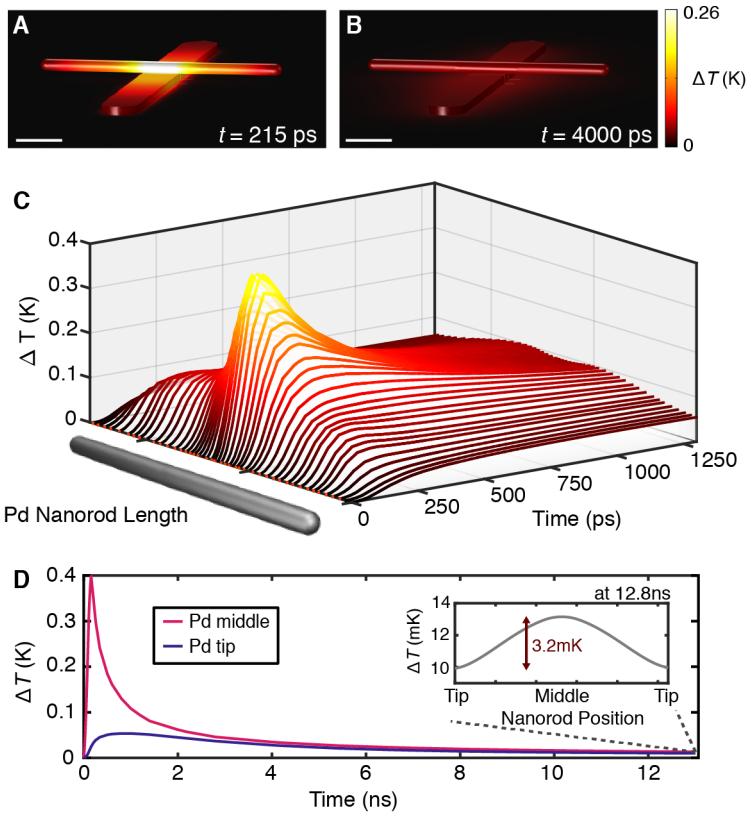

Figure S15: Finite element modeling of plasmon-induced heating in the Au-Pd structure. (A,B) Temperature distribution across the Au-Pd structure at 215ps (A) and after is has some time to equilibrate at 4ns (B). Scale bars are 100nm. (C) The increase in temperature of the Pd nanorod after a pulse of resonant illumination at t_0=100ps as a function of both time and nanorod length. The peak temperature increase is at the middle of the nanorod between the two EM hot spots, which then relaxes and thermalizes across the nanorod. (D) The temperature response of the Pd nanorod middle (pink) versus tip (blue) as a function of time. These are linecuts from (C) but plotted over the full temporal range. At 12.8ns (inset), the temperature difference between the middle and tip is 3.2mK.

second. However, this gives us an unphysical temperature difference of 2.5 $\times 10^5$K. This also does not make mathematical sense as there are additional pathways for heat loss (e.g. natural convection, radiation) that are not accounted for in our heating simulations. We do not see any melting in either our Pd nanorods nor the Au nanobar, suggesting that we have not reached either of their melting temperatures (1337K for Au and 1591K for Pd). Additionally, in our illumination studies which span around 180s of continuous illumination, we see about ∼50nm of drift over the course of 180s. Since our heating area is around $100 \times 100 \mu m^2$ (the area of the patterned Au nanobar array), this is similar to heating in TEM holders via a MEMS chip. According to Protochips' Fusion holder specifications, a ∼ 500K increase can correspond to 180nm of drift within 1 minute, implying that we probably also have less than a 500K temperature increase. However, we note that this is a much higher upper-bound than the expected heating in the system.

2.13 Raw Molecular Dynamics Results

As seen in Figure S16, the Gibbs free energy of various α-β distributions is plotted in order of increasing energy for the three different lengths. We note that just looking at the lowest energy configuration does not tell us anything about preferred reaction paths; instead, we need to think about the energy difference between our starting configuration (fully β-phase) and the different possible configurations.

Note that these calculations also support tip-nucleation dynamics seen in the hydrogenation of Pd nanorods (*16*). Since hydrogenation is exactly opposite of dehydrogenation, the middle-nucleation

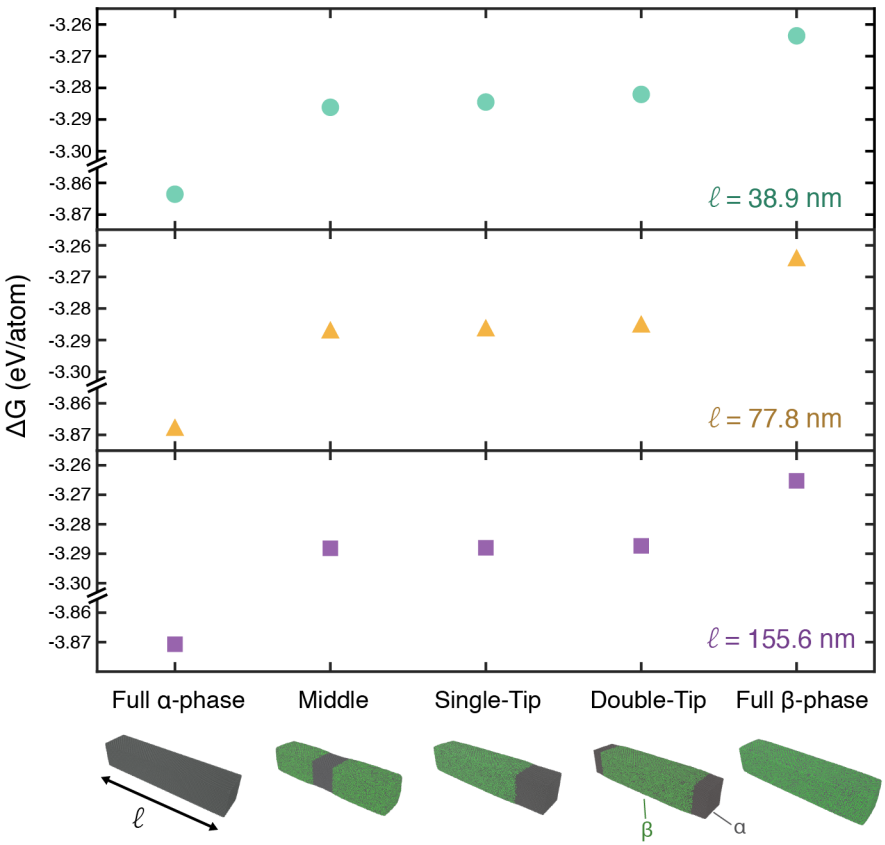

Figure S16: Raw data for Gibbs free energy for various nanorod configurations. Calculated Gibbs free energy using molecular dynamics for various nanobar α-β configurations for nanobar lengths 38.9nm (aqua, top), 77.8nm (yellow, middle), and 155.6nm (purple, bottom). The percentage of the particle in α-phase is exaggerated in the schematics to aid with visualization. The configurations are listed in order of lowest to highest Gibbs free energy, and the order is consistent for all lengths.

dehydrogenation case is exactly the same as the double-tip hydrogenation case. Here, we also see that double-tip hydrogenation (i.e. middle-nucleation dehydrogenation) is closest in energy to the full α-phase nanobar, similarly indicating that hydrogenation should also prefer tip-nucleation dynamics.

3 Supplementary movies

Movie S1. Movie file for the dehydrogenation seen in Figure 2D. Video file starts when the laser is turned on. Scale bar is 100nm.

References and Notes

1. Y. Liu, G. Zhou, K. Liu, Y. Cui, Design of complex nanomaterials for energy storage: Past success and future opportunity. *Acc. Chem. Res.* **50**, 2895–2905 (2017). doi:10.1021/acs.accounts.7b00450 Medline

2. M. Wuttig, H. Bhaskaran, T. Taubner, Phase-change materials for non-volatile photonic applications. *Nat. Photonics* **11**, 465–476 (2017). doi:10.1038/nphoton.2017.126

3. F. F. Tao, P. A. Crozier, Atomic-scale observations of catalyst structures under reaction conditions and during catalysis. *Chem. Rev.* **116**, 3487–3539 (2016). doi:10.1021/cr5002657 Medline

4. Y. Niu, X. Liu, Y. Wang, S. Zhou, Z. Lv, L. Zhang, W. Shi, Y. Li, W. Zhang, D. S. Su, B. Zhang, Visualizing formation of intermetallic PdZn in a palladium/zinc oxide catalyst: Interfacial fertilization by PdH_x. *Angew. Chem. Int. Ed.* **58**, 4232–4237 (2019). doi:10.1002/anie.201812292 Medline

5. X. Zhang, S. Han, B. Zhu, G. Zhang, X. Li, Y. Gao, Z. Wu, B. Yang, Y. Liu, W. Baaziz, O. Ersen, M. Gu, J. Miller, W. Liu, Reversible loss of core–shell structure for Ni-Au bimetallic nanoparticles during CO_2 hydrogenation. *Nat. Catal.* **3**, 411–417 (2020). doi:10.1038/s41929-020-0440-2

6. E. Cortés, W. Xie, J. Cambiasso, A. S. Jermyn, R. Sundararaman, P. Narang, S. Schlücker, S. A. Maier, Plasmonic hot electron transport drives nano-localized chemistry. *Nat. Commun.* **8**, 14880 (2017). doi:10.1038/ncomms14880 Medline

7. W. D. Yang, C. Wang, L. A. Fredin, P. A. Lin, L. Shimomoto, H. J. Lezec, R. Sharma, Site-selective CO disproportionation mediated by localized surface plasmon resonance excited by electron beam. *Nat. Mater.* **18**, 614–619 (2019). doi:10.1038/s41563-019-0342-3 Medline

8. H. Fujiwara, T. Suzuki, C. Pin, K. Sasaki, Localized ZnO growth on a gold nano-antenna by plasmon-assisted hydrothermal synthesis. *Nano Lett.* **20**, 389–394 (2020). doi:10.1021/acs.nanolett.9b04073 Medline

9. L. Zhou, D. F. Swearer, C. Zhang, H. Robatjazi, H. Zhao, L. Henderson, L. Dong, P. Christopher, E. A. Carter, P. Nordlander, N. J. Halas, Quantifying hot carrier and thermal contributions in plasmonic photocatalysis. *Science* **362**, 69–72 (2018). doi:10.1126/science.aat6967 Medline

10. J. Gargiulo, R. Berté, Y. Li, S. A. Maier, E. Cortés, From optical to chemical hot spots in plasmonics. *Acc. Chem. Res.* **52**, 2525–2535 (2019). doi:10.1021/acs.accounts.9b00234 Medline

11. N. Zou, G. Chen, X. Mao, H. Shen, E. Choudhary, X. Zhou, P. Chen, Imaging catalytic hotspots on single plasmonic nanostructures via correlated super-resolution and electron microscopy. *ACS Nano* **12**, 5570–5579 (2018). doi:10.1021/acsnano.8b01338 Medline

12. M. Vadai, D. K. Angell, F. Hayee, K. Sytwu, J. A. Dionne, In-situ observation of plasmon-controlled photocatalytic dehydrogenation of individual palladium nanoparticles. *Nat. Commun.* **9**, 4658 (2018). doi:10.1038/s41467-018-07108-x Medline

13. A. Stolaś, I. Darmadi, F. A. A. Nugroho, K. Moth-Poulsen, C. Langhammer, Impact of surfactants and stabilizers on palladium nanoparticle-hydrogen interaction kinetics: Implications for hydrogen sensors. *ACS Appl. Nano Mater.* **3**, 2647–2653 (2020). doi:10.1021/acsanm.0c00020

14. T. B. Flanagan, W. Luo, J. D. Clewley, Calorimetric enthalpies of absorption and desorption of protium and deuterium by palladium. *J. Less Common Met.* **172–174**, 42–55 (1991). doi:10.1016/0022-5088(91)90431-3

15. K. Sytwu, F. Hayee, T. C. Narayan, A. L. Koh, R. Sinclair, J. A. Dionne, Visualizing facet-dependent hydrogenation dynamics in individual palladium nanoparticles. *Nano Lett.* **18**, 5357–5363 (2018). doi:10.1021/acs.nanolett.8b00736 Medline

16. F. Hayee, T. C. Narayan, N. Nadkarni, A. Baldi, A. L. Koh, M. Z. Bazant, R. Sinclair, J. A. Dionne, In-situ visualization of solute-driven phase coexistence within individual nanorods. *Nat. Commun.* **9**, 1775 (2018). doi:10.1038/s41467-018-04021-1 Medline

17. T. Yokosawa, T. Alan, G. Pandraud, B. Dam, H. Zandbergen, In-situ TEM on (de)hydrogenation of Pd at 0.5–4.5 bar hydrogen pressure and 20–400°C. *Ultramicroscopy* **112**, 47–52 (2012). doi:10.1016/j.ultramic.2011.10.010 Medline

18. V. A. Spata, E. A. Carter, Mechanistic insights into photocatalyzed hydrogen desorption from palladium surfaces assisted by localized surface plasmon resonances. *ACS Nano* **12**, 3512–3522 (2018). doi:10.1021/acsnano.8b00352 Medline

19. W. E. Vargas, I. Rojas, D. E. Azofeifa, N. Clark, Optical and electrical properties of hydrided palladium thin films studied by an inversion approach from transmittance measurements. *Thin Solid Films* **496**, 189–196 (2006). doi:10.1016/j.tsf.2005.08.346

20. Y. Tang, R. E. Edelmann, S. Zou, Length tunable penta-twinned palladium nanorods: Seedless synthesis and electrooxidation of formic acid. *Nanoscale* **6**, 5630–5633 (2014). doi:10.1039/c4nr00299g Medline

21. T. C. Narayan, F. Hayee, A. Baldi, A. Leen Koh, R. Sinclair, J. A. Dionne, Direct visualization of hydrogen absorption dynamics in individual palladium nanoparticles. *Nat. Commun.* **8**, 14020 (2017). doi:10.1038/ncomms14020 Medline

22. N. J. J. Johnson, B. Lam, B. P. MacLeod, R. S. Sherbo, M. Moreno-Gonzalez, D. K. Fork, C. P. Berlinguette, Facets and vertices regulate hydrogen uptake and release in palladium nanocrystals. *Nat. Mater.* **18**, 454–458 (2019). doi:10.1038/s41563-019-0308-5 Medline

23. R. Griessen, N. Strohfeldt, H. Giessen, Thermodynamics of the hybrid interaction of hydrogen with palladium nanoparticles. *Nat. Mater.* **15**, 311–317 (2016). doi:10.1038/nmat4480 Medline

24. G. Baffou, *Thermoplasmonics: Heating Metal Nanoparticles Using Light* (Cambridge Univ. Press, 2017).

25. X. W. Zhou, J. A. Zimmerman, B. M. Wong, J. J. Hoyt, An embedded-atom method interatomic potential for Pd-H alloys. *J. Mater. Res.* **23**, 704–718 (2008). doi:10.1557/JMR.2008.0090

26. S. J. Madsen, M. Esfandyarpour, M. L. Brongersma, R. Sinclair, Observing plasmon damping due to adhesion layers in gold nanostructures using electron energy loss

spectroscopy. *ACS Photonics* **4**, 268–274 (2017). doi:10.1021/acsphotonics.6b00525 Medline

27. P. K. Ghosh, D. T. Debu, D. A. French, J. B. Herzog, Calculated thickness dependent plasmonic properties of gold nanobars in the visible to near-infrared light regime. *PLOS ONE* **12**, e0177463 (2017). doi:10.1371/journal.pone.0177463 Medline